

Measurement of the $t\bar{t}$ cross section using high-multiplicity jet events

V.M. Abazov³⁷, B. Abbott⁷⁵, M. Abolins⁶⁵, B.S. Acharya³⁰, M. Adams⁵¹, T. Adams⁴⁹, E. Aguilo⁶, M. Ahsan⁵⁹, G.D. Alexeev³⁷, G. Alkhazov⁴¹, A. Alton^{64,a}, G. Alverson⁶³, G.A. Alves², L.S. Ancu³⁶, M. Aoki⁵⁰, Y. Arnaud¹⁴, M. Arov⁶⁰, A. Askew⁴⁹, B. Åsman⁴², O. Atramentov^{49,b}, C. Avila⁸, J. BackusMayes⁸², F. Badaud¹³, L. Bagby⁵⁰, B. Baldin⁵⁰, D.V. Bandurin⁵⁹, S. Banerjee³⁰, E. Barberis⁶³, A.-F. Barfuss¹⁵, P. Baringer⁵⁸, J. Barreto², J.F. Bartlett⁵⁰, U. Bassler¹⁸, D. Bauer⁴⁴, S. Beale⁶, A. Bean⁵⁸, M. Begalli³, M. Begel⁷³, C. Belanger-Champagne⁴², L. Bellantoni⁵⁰, J.A. Benitez⁶⁵, S.B. Beri²⁸, G. Bernardi¹⁷, R. Bernhard²³, I. Bertram⁴³, M. Besançon¹⁸, R. Beuselinck⁴⁴, V.A. Bezzubov⁴⁰, P.C. Bhat⁵⁰, V. Bhatnagar²⁸, G. Blazey⁵², S. Blessing⁴⁹, K. Bloom⁶⁷, A. Boehnlein⁵⁰, D. Boline⁶², T.A. Bolton⁵⁹, E.E. Boos³⁹, G. Borissov⁴³, T. Bose⁶², A. Brandt⁷⁸, R. Brock⁶⁵, G. Brooijmans⁷⁰, A. Bross⁵⁰, D. Brown¹⁹, X.B. Bu⁷, D. Buchholz⁵³, M. Buehler⁸¹, V. Buescher²⁵, V. Bunichev³⁹, S. Burdin^{43,c}, T.H. Burnett⁸², C.P. Buszello⁴⁴, P. Calfayan²⁶, B. Calpas¹⁵, S. Calvet¹⁶, E. Camacho-Pérez³⁴, J. Cammin⁷¹, M.A. Carrasco-Lizarraga³⁴, E. Carrera⁴⁹, W. Carvalho³, B.C.K. Casey⁵⁰, H. Castilla-Valdez³⁴, S. Chakrabarti⁷², D. Chakraborty⁵², K.M. Chan⁵⁵, A. Chandra⁵⁴, E. Cheu⁴⁶, S. Chevalier-Théry¹⁸, D.K. Cho⁶², S.W. Cho³², S. Choi³³, B. Choudhary²⁹, T. Christoudias⁴⁴, S. Cihangir⁵⁰, D. Claes⁶⁷, J. Clutter⁵⁸, M. Cooke⁵⁰, W.E. Cooper⁵⁰, M. Corcoran⁸⁰, F. Couderc¹⁸, M.-C. Cousinou¹⁵, D. Cutts⁷⁷, M. Ćwiok³¹, A. Das⁴⁶, G. Davies⁴⁴, K. De⁷⁸, S.J. de Jong³⁶, E. De La Cruz-Burelo³⁴, K. DeVaughan⁶⁷, F. Déliot¹⁸, M. Demarteau⁵⁰, R. Demina⁷¹, D. Denisov⁵⁰, S.P. Denisov⁴⁰, S. Desai⁵⁰, H.T. Diehl⁵⁰, M. Diesburg⁵⁰, A. Dominguez⁶⁷, T. Dorland⁸², A. Dubey²⁹, L.V. Dudko³⁹, L. Duflot¹⁶, D. Duggan⁴⁹, A. Duperrin¹⁵, S. Dutt²⁸, A. Dyshkant⁵², M. Eads⁶⁷, D. Edmunds⁶⁵, J. Ellison⁴⁸, V.D. Elvira⁵⁰, Y. Enari¹⁷, S. Eno⁶¹, H. Evans⁵⁴, A. Evdokimov⁷³, V.N. Evdokimov⁴⁰, G. Facini⁶³, A.V. Ferapontov⁷⁷, T. Ferbel^{61,71}, F. Fiedler²⁵, F. Filthaut³⁶, W. Fisher⁵⁰, H.E. Fisk⁵⁰, M. Fortner⁵², H. Fox⁴³, S. Fuess⁵⁰, T. Gadfort⁷⁰, C.F. Galea³⁶, A. Garcia-Bellido⁷¹, V. Gavrilov³⁸, P. Gay¹³, W. Geist¹⁹, W. Geng^{15,65}, D. Gerbaudo⁶⁸, C.E. Gerber⁵¹, Y. Gershtein^{49,b}, D. Gillberg⁶, G. Ginther^{50,71}, G. Golovanov³⁷, B. Gómez⁸, A. Goussiou⁸², P.D. Grannis⁷², S. Greder¹⁹, H. Greenlee⁵⁰, Z.D. Greenwood⁶⁰, E.M. Gregores⁴, G. Grenier²⁰, Ph. Gris¹³, J.-F. Grivaz¹⁶, A. Grohsjean¹⁸, S. Grünendahl⁵⁰, M.W. Grünewald³¹, F. Guo⁷², J. Guo⁷², G. Gutierrez⁵⁰, P. Gutierrez⁷⁵, A. Haas^{70,d}, P. Haefner²⁶, S. Hagopian⁴⁹, J. Haley⁶³, I. Hall⁶⁵, R.E. Hall⁴⁷, L. Han⁷, K. Harder⁴⁵, A. Harel⁷¹, J.M. Hauptman⁵⁷, J. Hays⁴⁴, T. Hebbeker²¹, D. Hedin⁵², J.G. Hegeman³⁵, A.P. Heinson⁴⁸, U. Heintz⁶², C. Hensel²⁴, I. Heredia-De La Cruz³⁴, K. Herner⁶⁴, G. Hesketh⁶³, M.D. Hildreth⁵⁵, R. Hirosky⁸¹, T. Hoang⁴⁹, J.D. Hobbs⁷², B. Hoeneisen¹², H. Hoeth²⁷, M. Hohlfeld²⁵, S. Hossain⁷⁵, P. Houben³⁵, Y. Hu⁷², Z. Hubacek¹⁰, N. Huske¹⁷, V. Hynek¹⁰, I. Iashvili⁶⁹, R. Illingworth⁵⁰, A.S. Ito⁵⁰, S. Jabeen⁶², M. Jaffré¹⁶, S. Jain⁷⁵, K. Jakobs²³, D. Jamin¹⁵, R. Jesik⁴⁴, K. Johns⁴⁶, C. Johnson⁷⁰, M. Johnson⁵⁰, D. Johnston⁶⁷, A. Jonckheere⁵⁰, P. Jonsson⁴⁴, A. Juste⁵⁰, E. Kajfasz¹⁵, D. Karmanov³⁹, P.A. Kasper⁵⁰, I. Katsanos⁶⁷, V. Kaushik⁷⁸, R. Kehoe⁷⁹, S. Kermiche¹⁵, N. Khalatyan⁵⁰, A. Khanov⁷⁶, A. Kharchilava⁶⁹, Y.N. Kharzheev³⁷, D. Khatidze⁷⁷, M.H. Kirby⁵³, M. Kirsch²¹, J.M. Kohli²⁸, A.V. Kozelov⁴⁰, J. Kraus⁶⁵, A. Kumar⁶⁹, A. Kupco¹¹, T. Kurča²⁰, V.A. Kuzmin³⁹, J. Kvita⁹, F. Lacroix¹³, D. Lam⁵⁵, S. Lammers⁵⁴, G. Landsberg⁷⁷, P. Lebrun²⁰, H.S. Lee³², W.M. Lee⁵⁰, A. Leflat³⁹, J. Lellouch¹⁷, L. Li⁴⁸, Q.Z. Li⁵⁰, S.M. Lietti⁵, J.K. Lim³², D. Lincoln⁵⁰, J. Linnemann⁶⁵, V.V. Lipaev⁴⁰, R. Lipton⁵⁰, Y. Liu⁷, Z. Liu⁶, A. Lobodenko⁴¹, M. Lokajicek¹¹, P. Love⁴³, H.J. Lubatti⁸², R. Luna-Garcia^{34,e}, A.L. Lyon⁵⁰, A.K.A. Maciel², D. Mackin⁸⁰, P. Mättig²⁷, R. Magaña-Villalba³⁴, P.K. Mal⁴⁶, S. Malik⁶⁷, V.L. Malyshev³⁷, Y. Maravin⁵⁹, B. Martin¹⁴, J. Martínez-Ortega³⁴, R. McCarthy⁷², C.L. McGivern⁵⁸, M.M. Meijer³⁶, A. Melnitchouk⁶⁶, L. Mendoza⁸, D. Menezes⁵², P.G. Mercadante⁴, M. Merkin³⁹, A. Meyer²¹, J. Meyer²⁴, N.K. Mondal³⁰, R.W. Moore⁶, T. Moulik⁵⁸, G.S. Muanza¹⁵, M. Mulhearn⁸¹, O. Mundal²², L. Mundim³, E. Nagy¹⁵, M. Naimuddin²⁹, M. Narain⁷⁷, R. Nayyar²⁹, H.A. Neal⁶⁴, J.P. Negret⁸, P. Neustroev⁴¹, H. Nilsen²³, H. Nogima³, S.F. Novaes⁵, T. Nunnemann²⁶, G. Obrant⁴¹, D. Onoprienko⁵⁹, J. Orduna³⁴, N. Osman⁴⁴, J. Osta⁵⁵, R. Otec¹⁰, G.J. Otero y Garzón¹, M. Owen⁴⁵, M. Padilla⁴⁸, P. Padley⁸⁰, M. Pangilinan⁷⁷, N. Parashar⁵⁶, V. Parihar⁶², S.-J. Park²⁴, S.K. Park³², J. Parsons⁷⁰, R. Partridge⁷⁷, N. Parua⁵⁴, A. Patwa⁷³, B. Penning⁵⁰, M. Perfilov³⁹, K. Peters⁴⁵, Y. Peters⁴⁵, G. Petrillo⁷¹, P. Pétroff¹⁶, R. Piegaia¹, J. Piper⁶⁵, M.-A. Pleier⁷³, P.L.M. Podesta-Lerma^{34,f}, V.M. Podstavkov⁵⁰, Y. Pogorelov⁵⁵, M.-E. Pol², P. Polozov³⁸, A.V. Popov⁴⁰, M. Prewitt⁸⁰, S. Protopopescu⁷³, J. Qian⁶⁴, A. Quadt²⁴, B. Quinn⁶⁶, M.S. Rangel¹⁶, K. Ranjan²⁹, P.N. Ratoff⁴³, I. Razumov⁴⁰, P. Renkel⁷⁹, P. Rich⁴⁵, M. Rijssenbeek⁷², I. Ripp-Baudot¹⁹, F. Rizatdinova⁷⁶, S. Robinson⁴⁴, M. Rominsky⁷⁵, C. Royon¹⁸, P. Rubinov⁵⁰, R. Ruchti⁵⁵, G. Safronov³⁸, G. Sajot¹⁴, A. Sánchez-Hernández³⁴, M.P. Sanders²⁶, B. Sanghi⁵⁰, G. Savage⁵⁰, L. Sawyer⁶⁰, T. Scanlon⁴⁴, D. Schaile²⁶, R.D. Schamberger⁷², Y. Scheglov⁴¹, H. Schellman⁵³, T. Schliephake²⁷, S. Schlobohm⁸², C. Schwanenberger⁴⁵,

R. Schwienhorst⁶⁵, J. Sekaric⁵⁸, H. Severini⁷⁵, E. Shabalina²⁴, M. Shamim⁵⁹, V. Shary¹⁸, A.A. Shchukin⁴⁰, R.K. Shivpuri²⁹, V. Simak¹⁰, V. Sirotenko⁵⁰, P. Skubic⁷⁵, P. Slattery⁷¹, D. Smirnov⁵⁵, G.R. Snow⁶⁷, J. Snow⁷⁴, S. Snyder⁷³, S. Söldner-Rembold⁴⁵, L. Sonnenschein²¹, A. Sopczak⁴³, M. Sosebee⁷⁸, K. Soustruznik⁹, B. Spurlock⁷⁸, J. Stark¹⁴, V. Stolin³⁸, D.A. Stoyanova⁴⁰, J. Strandberg⁶⁴, M.A. Strang⁶⁹, E. Strauss⁷², M. Strauss⁷⁵, R. Ströhmer²⁶, D. Strom⁵¹, L. Stutte⁵⁰, S. Sumowidagdo⁴⁹, P. Svoisky³⁶, M. Takahashi⁴⁵, A. Tanasijczuk¹, W. Taylor⁶, B. Tiller²⁶, M. Titov¹⁸, V.V. Tokmenin³⁷, I. Torchiani²³, D. Tsybychev⁷², B. Tuchming¹⁸, C. Tully⁶⁸, P.M. Tuts⁷⁰, R. Unalan⁶⁵, L. Uvarov⁴¹, S. Uvarov⁴¹, S. Uzunyan⁵², P.J. van den Berg³⁵, R. Van Kooten⁵⁴, W.M. van Leeuwen³⁵, N. Varelas⁵¹, E.W. Varnes⁴⁶, I.A. Vasilyev⁴⁰, P. Verdier²⁰, L.S. Vertogradov³⁷, M. Verzocchi⁵⁰, M. Vesterinen⁴⁵, D. Vilanova¹⁸, P. Vint⁴⁴, P. Vokac¹⁰, R. Wagner⁶⁸, H.D. Wahl⁴⁹, M.H.L.S. Wang⁷¹, J. Warchol⁵⁵, G. Watts⁸², M. Wayne⁵⁵, G. Weber²⁵, M. Weber^{50,g}, A. Wenger^{23,h}, M. Wetstein⁶¹, A. White⁷⁸, D. Wicke²⁵, M.R.J. Williams⁴³, G.W. Wilson⁵⁸, S.J. Wimpenny⁴⁸, M. Wobisch⁶⁰, D.R. Wood⁶³, T.R. Wyatt⁴⁵, Y. Xie⁷⁷, C. Xu⁶⁴, S. Yacoub⁵³, R. Yamada⁵⁰, W.-C. Yang⁴⁵, T. Yasuda⁵⁰, Y.A. Yatsunenko³⁷, Z. Ye⁵⁰, H. Yin⁷, K. Yip⁷³, H.D. Yoo⁷⁷, S.W. Youn⁵⁰, J. Yu⁷⁸, C. Zeitnitz²⁷, S. Zelitch⁸¹, T. Zhao⁸², B. Zhou⁶⁴, J. Zhu⁷², M. Zielinski⁷¹, D. Zieminska⁵⁴, L. Zivkovic⁷⁰, V. Zutshi⁵², and E.G. Zverev³⁹

(The DØ Collaboration)

- ¹Universidad de Buenos Aires, Buenos Aires, Argentina
²LAFEX, Centro Brasileiro de Pesquisas Físicas, Rio de Janeiro, Brazil
³Universidade do Estado do Rio de Janeiro, Rio de Janeiro, Brazil
⁴Universidade Federal do ABC, Santo André, Brazil
⁵Instituto de Física Teórica, Universidade Estadual Paulista, São Paulo, Brazil
⁶University of Alberta, Edmonton, Alberta, Canada; Simon Fraser University, Burnaby, British Columbia, Canada; York University, Toronto, Ontario, Canada and McGill University, Montreal, Quebec, Canada
⁷University of Science and Technology of China, Hefei, People's Republic of China
⁸Universidad de los Andes, Bogotá, Colombia
⁹Center for Particle Physics, Charles University, Faculty of Mathematics and Physics, Prague, Czech Republic
¹⁰Czech Technical University in Prague, Prague, Czech Republic
¹¹Center for Particle Physics, Institute of Physics, Academy of Sciences of the Czech Republic, Prague, Czech Republic
¹²Universidad San Francisco de Quito, Quito, Ecuador
¹³LPC, Université Blaise Pascal, CNRS/IN2P3, Clermont, France
¹⁴LPSC, Université Joseph Fourier Grenoble 1, CNRS/IN2P3, Institut National Polytechnique de Grenoble, Grenoble, France
¹⁵CPPM, Aix-Marseille Université, CNRS/IN2P3, Marseille, France
¹⁶LAL, Université Paris-Sud, IN2P3/CNRS, Orsay, France
¹⁷LPNHE, IN2P3/CNRS, Universités Paris VI and VII, Paris, France
¹⁸CEA, Irfu, SPP, Saclay, France
¹⁹IPHC, Université de Strasbourg, CNRS/IN2P3, Strasbourg, France
²⁰IPNL, Université Lyon 1, CNRS/IN2P3, Villeurbanne, France and Université de Lyon, Lyon, France
²¹III. Physikalisches Institut A, RWTH Aachen University, Aachen, Germany
²²Physikalisches Institut, Universität Bonn, Bonn, Germany
²³Physikalisches Institut, Universität Freiburg, Freiburg, Germany
²⁴II. Physikalisches Institut, Georg-August-Universität Göttingen, Göttingen, Germany
²⁵Institut für Physik, Universität Mainz, Mainz, Germany
²⁶Ludwig-Maximilians-Universität München, München, Germany
²⁷Fachbereich Physik, University of Wuppertal, Wuppertal, Germany
²⁸Panjab University, Chandigarh, India
²⁹Delhi University, Delhi, India
³⁰Tata Institute of Fundamental Research, Mumbai, India
³¹University College Dublin, Dublin, Ireland
³²Korea Detector Laboratory, Korea University, Seoul, Korea
³³SungKyunKwan University, Suwon, Korea
³⁴CINVESTAV, Mexico City, Mexico
³⁵FOM-Institute NIKHEF and University of Amsterdam/NIKHEF, Amsterdam, The Netherlands
³⁶Radboud University Nijmegen/NIKHEF, Nijmegen, The Netherlands
³⁷Joint Institute for Nuclear Research, Dubna, Russia
³⁸Institute for Theoretical and Experimental Physics, Moscow, Russia
³⁹Moscow State University, Moscow, Russia
⁴⁰Institute for High Energy Physics, Protvino, Russia

- ⁴¹*Petersburg Nuclear Physics Institute, St. Petersburg, Russia*
⁴²*Stockholm University, Stockholm, Sweden, and Uppsala University, Uppsala, Sweden*
⁴³*Lancaster University, Lancaster, United Kingdom*
⁴⁴*Imperial College London, London SW7 2AZ, United Kingdom*
⁴⁵*The University of Manchester, Manchester M13 9PL, United Kingdom*
⁴⁶*University of Arizona, Tucson, Arizona 85721, USA*
⁴⁷*California State University, Fresno, California 93740, USA*
⁴⁸*University of California, Riverside, California 92521, USA*
⁴⁹*Florida State University, Tallahassee, Florida 32306, USA*
⁵⁰*Fermi National Accelerator Laboratory, Batavia, Illinois 60510, USA*
⁵¹*University of Illinois at Chicago, Chicago, Illinois 60607, USA*
⁵²*Northern Illinois University, DeKalb, Illinois 60115, USA*
⁵³*Northwestern University, Evanston, Illinois 60208, USA*
⁵⁴*Indiana University, Bloomington, Indiana 47405, USA*
⁵⁵*University of Notre Dame, Notre Dame, Indiana 46556, USA*
⁵⁶*Purdue University Calumet, Hammond, Indiana 46323, USA*
⁵⁷*Iowa State University, Ames, Iowa 50011, USA*
⁵⁸*University of Kansas, Lawrence, Kansas 66045, USA*
⁵⁹*Kansas State University, Manhattan, Kansas 66506, USA*
⁶⁰*Louisiana Tech University, Ruston, Louisiana 71272, USA*
⁶¹*University of Maryland, College Park, Maryland 20742, USA*
⁶²*Boston University, Boston, Massachusetts 02215, USA*
⁶³*Northeastern University, Boston, Massachusetts 02115, USA*
⁶⁴*University of Michigan, Ann Arbor, Michigan 48109, USA*
⁶⁵*Michigan State University, East Lansing, Michigan 48824, USA*
⁶⁶*University of Mississippi, University, Mississippi 38677, USA*
⁶⁷*University of Nebraska, Lincoln, Nebraska 68588, USA*
⁶⁸*Princeton University, Princeton, New Jersey 08544, USA*
⁶⁹*State University of New York, Buffalo, New York 14260, USA*
⁷⁰*Columbia University, New York, New York 10027, USA*
⁷¹*University of Rochester, Rochester, New York 14627, USA*
⁷²*State University of New York, Stony Brook, New York 11794, USA*
⁷³*Brookhaven National Laboratory, Upton, New York 11973, USA*
⁷⁴*Langston University, Langston, Oklahoma 73050, USA*
⁷⁵*University of Oklahoma, Norman, Oklahoma 73019, USA*
⁷⁶*Oklahoma State University, Stillwater, Oklahoma 74078, USA*
⁷⁷*Brown University, Providence, Rhode Island 02912, USA*
⁷⁸*University of Texas, Arlington, Texas 76019, USA*
⁷⁹*Southern Methodist University, Dallas, Texas 75275, USA*
⁸⁰*Rice University, Houston, Texas 77005, USA*
⁸¹*University of Virginia, Charlottesville, Virginia 22901, USA and*
⁸²*University of Washington, Seattle, Washington 98195, USA*

(Dated: November 22, 2009)

We present a measurement of the $t\bar{t}$ cross section using high-multiplicity jet events produced in $p\bar{p}$ collisions at $\sqrt{s} = 1.96$ TeV. These data were recorded at the Fermilab Tevatron collider with the D0 detector. Events with at least six jets, two of them identified as b jets, were selected from a 1 fb^{-1} data set. The measured cross section, assuming a top quark mass of $175 \text{ GeV}/c^2$, is $6.9 \pm 2.0 \text{ pb}$, in agreement with theoretical expectations.

PACS numbers: 14.65.Ha

I. INTRODUCTION

The top quark is the most massive fundamental particle ever observed. Its mass, $m_t = 173.1 \pm 1.3 \text{ GeV}/c^2$ [1], is approximately twice that of the next heaviest elementary particle, the Z boson, and is approximately 35 times that of its weak-isospin partner, the bottom quark. Top quarks are primarily produced in pairs at the Fermilab Tevatron $p\bar{p}$ collider via the $q\bar{q} \rightarrow t\bar{t}$ ($\approx 85\%$) and $gg \rightarrow t\bar{t}$ ($\approx 15\%$) quantum chromodynamic (QCD) pro-

cesses. They decay to a W boson and a b quark with a branching fraction near one according to the standard model (SM). The W boson subsequently decays into a lepton and a neutrino or into a quark-antiquark pair. The decay products of the W bosons are used to classify the top quark decay channel. The all-hadronic decay channel, with a branching fraction of 46% [2], has a final state containing two b quarks and four lighter quarks and is shown schematically in Fig. 1. The top quark might also decay into non-SM particles (e.g., a charged

Higgs boson) and the decay products of these new particles can change the branching fractions of the leptonic and all-hadronic $t\bar{t}$ decay channels [3]. Comparing the $t\bar{t}$ production cross section between different decay channels directly constrains the existence of beyond the standard model particles lighter than the top quark.

In this paper, we present a new measurement of the $p\bar{p} \rightarrow t\bar{t} + X$ cross section using events containing at least six jets, two of them identified as b jets. The data sample corresponds to $\approx 1 \text{ fb}^{-1}$ acquired by the D0 experiment at a center-of-mass energy $\sqrt{s} = 1.96 \text{ TeV}$. D0 previously published a measurement of the $t\bar{t}$ cross section in multi-jet events with 0.4 fb^{-1} of integrated luminosity and obtained $4.5_{-1.9}^{+2.0} (\text{stat.})_{-1.1}^{+1.4} (\text{sys.}) \pm 0.3 (\text{lum.}) \text{ pb}$ [4]. CDF published a similar measurement with 1 fb^{-1} and obtained $8.3 \pm 1.0 (\text{stat.})_{-1.5}^{+2.0} (\text{sys.}) \pm 0.5 (\text{lum.}) \text{ pb}$ [5]. Both measurements assumed $m_t = 175 \text{ GeV}/c^2$ and agree with the cross section measurement presented in this paper and with the SM expectation of $6.90_{-0.62}^{+0.44} \text{ pb}$ [6, 7].

The dominant source of background in the all-hadronic channel is QCD multijet production. Rather than relying on event generators such as PYTHIA [8], HERWIG [9], or ALPGEN [10] to reproduce all characteristics of events with six or more jets, we instead derived a background sample from the triggered data (Sec. III B). The background was suppressed compared to signal by requiring at least two of the jets be identified as b jets (Sec. II E). The $t\bar{t}$ signal was simulated by the ALPGEN event generator that used PYTHIA with the tune A [11] parameter settings for the parton shower, hadronization, and underlying event aspects. Kinematic selection criteria were applied to further improve the signal-to-background ratio to approximately 1 : 7 (Sec. III D). The $t\bar{t}$ production cross section was extracted using signal and background templates for a likelihood discriminant constructed from topological and kinematic observables. (Sec. IV).

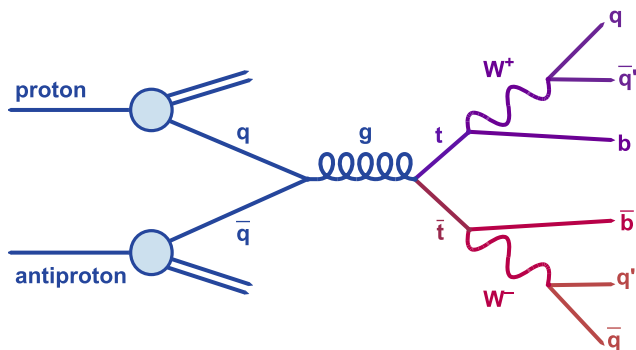


FIG. 1: Dominant Feynman diagram for $t\bar{t}$ production in the all-hadronic decay channel. The t decays into a W^+b and the W^+ decays into either $u\bar{d}$ or $c\bar{s}$ (represented by the q and \bar{q}' in the figure); the \bar{t} and W^- decay into the charge conjugates. The event signature consists of two b jets and at least four other jets.

II. DETECTOR AND RECONSTRUCTION

A. Detector

The D0 detector [12] has a central-tracking system consisting of a silicon microstrip tracker (SMT) and a central fiber tracker (CFT), both located within a 2 T superconducting solenoidal magnet, with designs optimized for tracking and vertexing at pseudorapidities $|\eta| < 3$ and $|\eta| < 2.5$, respectively [13]. Central and forward preshower detectors are positioned just outside of the superconducting coil. The liquid-argon and uranium calorimeter has a central section (CC) covering pseudorapidities $|\eta| \lesssim 1.1$ and two end calorimeters (EC) that extend coverage to $|\eta| \approx 4.2$, with all three housed in separate cryostats [14]. Each calorimeter contains a four-layer electromagnetic (EM) section closest to the interaction region, followed by finely- and coarsely-segmented hadronic sections. Scintillators between the CC and EC cryostats provide sampling of developing showers at $1.1 \lesssim |\eta| \lesssim 1.4$. The luminosity is measured using scintillators placed in front of the EC cryostats [15]. An outer muon system, covering $|\eta| < 2$, consists of a layer of tracking detectors and scintillation trigger counters in front of 1.8 T iron toroids, followed by two similar layers beyond the toroids. The trigger and data acquisition systems were designed to accommodate the high luminosities of Tevatron Run II.

B. Trigger

The events used in this analysis were collected using a multijet trigger. The first level of the trigger used dedicated hardware and preliminary information from the calorimeter to identify multijet events. This selection was refined in a second level with more complex algorithms. The third trigger level employed a fast reconstruction of the event with a simple cone jet algorithm [16]. This selection was further refined using the final reconstruction algorithms which included the midpoint cone jet algorithm [16]. Kinematic and jet multiplicity requirements were applied at each stage to reduce the overall data rate.

The trigger required at least four reconstructed jets. The specific requirements on the jets, particularly the energy thresholds, were changed several times during data collection to cope with the increasing instantaneous luminosity delivered by the Tevatron. Efficiencies were measured independently for each trigger epoch and combined together weighted by the integrated luminosity of each epoch. Rather than correcting the data for inefficiencies in the trigger, the simulated $t\bar{t}$ signal was weighted by the trigger efficiency. The average trigger efficiency for $t\bar{t}$ signal events that passed all selection criteria used in this analysis is shown in Fig. 2 as a function of H_T where $H_T = \sum p_T$ over all jets and p_T is the transverse momentum of a jet. The background sample was created from the triggered data (see Sec. III B) and therefore need no

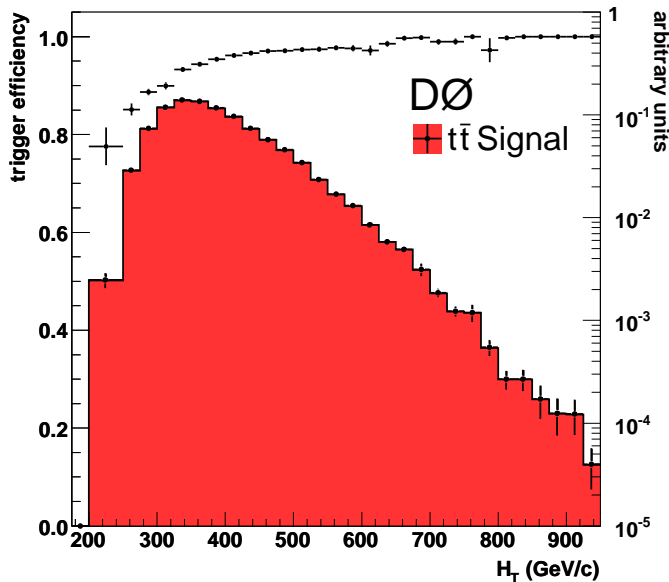


FIG. 2: Average trigger efficiency for simulated all-hadronic $t\bar{t}$ events as a function of H_T . The untriggered $t\bar{t}$ H_T distribution, normalized to unit area, is also shown (scale shown on the right.) Displayed error bars represent statistical uncertainties only.

additional corrections.

C. Tracks and Vertices

Tracks were reconstructed from hit information in the SMT and CFT. The location of the hard-scatter interaction point was reconstructed by means of an adaptive primary vertex algorithm [17, 18]. Only vertices constructed from at least three tracks were considered in this analysis; $\mathcal{O}(40)$ tracks are associated, on average, with primary vertices in simulated all-hadronic $t\bar{t}$ events. A distribution of the location of primary vertices along the z axis in triggered events is displayed in Fig. 3. The primary interaction vertex was required to be within 35 cm of the center of the detector along the z axis to keep it within the fiducial volume of the SMT [18]. The distribution in Fig. 3 was fitted within the $|z_{PV}| < 35$ cm range with the sum of two Gaussians. The fit extrapolation outside this range is also shown. The total primary vertex acceptance was $79.5 \pm 2.0\%$.

D. Jets

Jets were reconstructed from energy deposits in calorimeter cells using the Run II midpoint cone algorithm [16] with a cone radius $\mathcal{R} = \sqrt{(\Delta\phi)^2 + (\Delta y)^2} = 0.5$ [19]. Noisy calorimeter cells were suppressed by only including cells that had energies $\geq 4\sigma$ above the average electronic noise and that also had adjacent cells with

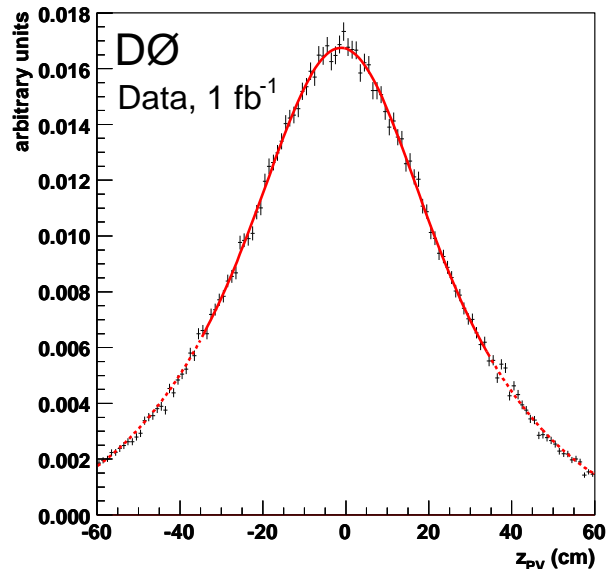


FIG. 3: The distribution of the primary vertex z position with respect to the center of the detector in the triggered data. The solid line is a fit to the region with $|z_{PV}| < 35$ cm, while the dotted line is an extrapolation of the fit outside that region. Displayed error bars represent statistical uncertainties only. The distribution is normalized to unit area.

energies $\geq 2\sigma$ above noise. Jets were required to have $< 40\%$ of their energy in the coarse hadronic calorimeter, have at least half the remaining transverse energy matched to energy depositions identified by the hardware trigger, and have between 5% and 95% of their energy in the EM calorimeter. These requirements were for jets reconstructed in the CC; they were looser at forward rapidities.

Jet energies were corrected for the energy response of the calorimeter, for the effect of particles showering outside the jet cone, for overlaps due to multiple interactions and event pile-up, and for calorimeter noise [20]. The calorimeter response was measured using the p_T imbalance in γ +jet and dijet events; the response of the calorimeter to electromagnetic showers was calibrated using the $Z \rightarrow e^+e^-$ mass peak and a detailed accounting of the material between the calorimeter and the interaction point. The jet energy calibration also used Z +jet events and events acquired using low bias triggers. Jets that contained muons, assumed to originate from c - or b -hadron decays, were corrected to account for the energy of the muon and the accompanying neutrino. Muons with $p_T > 60$ GeV/ c were treated as having $p_T = 60$ GeV/ c to avoid the impact from poorly reconstructed muon momenta. Jet energies were calibrated independently in the data and in the simulation using the same methodology. Jets in the simulation required additional corrections to reproduce the reconstruction efficiency and energy resolution in the data. The uncertainty on the jet energy calibration is $\approx 1.5\%$.

Jets were further required to be matched with at least

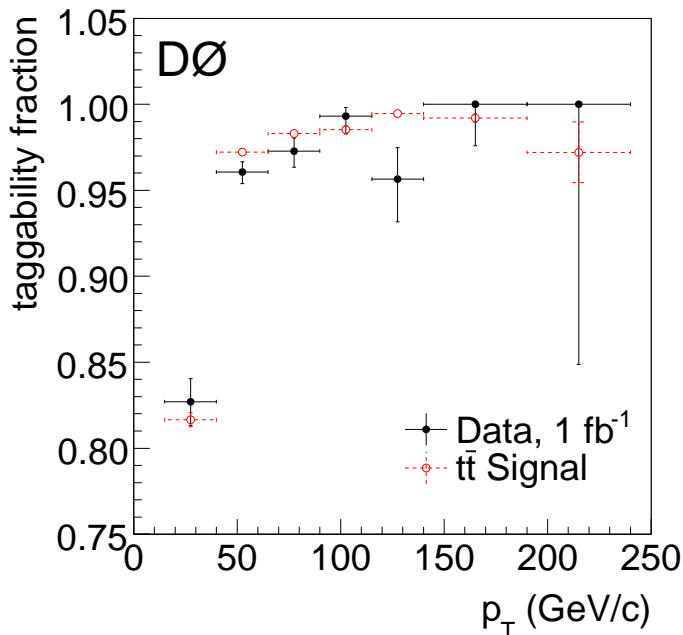


FIG. 4: Comparison of taggability fraction in selected multijet data after selection with that in the $t\bar{t}$ simulation as a function of jet p_T . Displayed error bars represent statistical uncertainties only.

two good quality tracks having $p_T > 1$ GeV/ c and $p_T > 0.5$ GeV/ c , respectively, that included SMT hits and pointed to the primary vertex. These requirements are termed “taggability” and are important for identifying heavy-flavor jets (Sec. II E) and to reject jets produced by overlapping $p\bar{p}$ collisions. The taggability fraction depends nominally on the jet p_T , jet rapidity, z_{PV} , $\text{sign}(z_{PV} \times \eta_{\text{jet}}) \times |z_{PV}|$, and the flavor of the jet [18]. The fraction of jets that were taggable was measured using the selected sample of multijet events (Sec. III D) and is shown in Fig. 4 binned in jet p_T . Differences between the taggability determined with multijet data and with the $t\bar{t}$ signal simulation could bias the cross section measurement. The $t\bar{t}$ simulation yielded the same taggability fraction as a function of jet p_T and η as the multijet data within the statistical uncertainties (Fig. 4). The uncertainty on the relative difference between data and simulation is 2% and is dominated by the limited statistics in the comparison.

E. b Jets

Jets that contain a b hadron are called “ b jets” as they typically originate from a b quark. b hadrons have relatively long lifetimes and so usually travel several millimeters before they decay. Secondary vertices, displaced from the primary vertex, are usually formed by the tracks associated with the decay products of the b hadron.

An artificial neural network (NN) was used to identify b jets [21]. Selected characteristics of secondary ver-

tices and tracks associated with b hadron decays were used as inputs to the NN. These included aspects of the secondary vertex such as its decay length significance, goodness of fit, number of tracks, mass of the system of particles associated with the vertex, and the number of secondary vertices found in the jet. Additionally, the weighted combination of track impact parameter significances and the probability that the jet originated from the primary vertex were also input into the NN.

The probability to identify a b jet, the tag rate function, was measured in data and parametrized as a function of the jet p_T and η . Similar functions were determined for charm jets. The fake rate, the probability to assign a b tag to a non- b jet, was dominated by light jets and long-lived particles (e.g., K_s^0 , Λ^0). The b -tagging efficiency is $(57 \pm 2)\%$, the tagging efficiency for charm is $(15 \pm 1)\%$, and the fake rate is $(0.57 \pm 0.07)\%$ for the NN output threshold used in this analysis at $p_T = 40$ GeV/ c [21].

III. ANALYSIS TECHNIQUES

A. Data Sample

The data used for this analysis were collected between August 2002 and February 2006 with the four-jet trigger described in Sec. II B. Quality requirements were imposed on the selected data; runs or parts of runs in which detector systems essential to this analysis had problems or significant noise were discarded. The integrated luminosity of the data sample, including these trigger and quality requirements, is 0.97 ± 0.06 fb $^{-1}$.

B. Background Model

QCD multijet events that have at least two heavy-flavor jets are the dominant source of background to $t\bar{t}$ production in the all-hadronic decay channel. This large background is distinguished from the $t\bar{t}$ signal by exploiting differences between the kinematic and topological distributions of jets in $t\bar{t}$ and multijet events. Correlations between jets, particularly for b jets, must be reproduced for the observables used in this analysis.

The background sample was created using triggered data events. Signal contamination in the background sample was minimized by selecting events with two b -tagged jets and low jet multiplicities. Samples of events with at least four taggable jets having $p_T > 15$ GeV/ c were selected from the triggered data. The b -jet identification criteria described in Sec. II E were applied to these samples; events were kept if there were at least two tagged jets. The background sample was then created by attaching low- p_T jets selected from events with six or more jets to events with four or five jets. A reasonable distribution of the jets in the available phase space was ensured using a set of matching criteria.

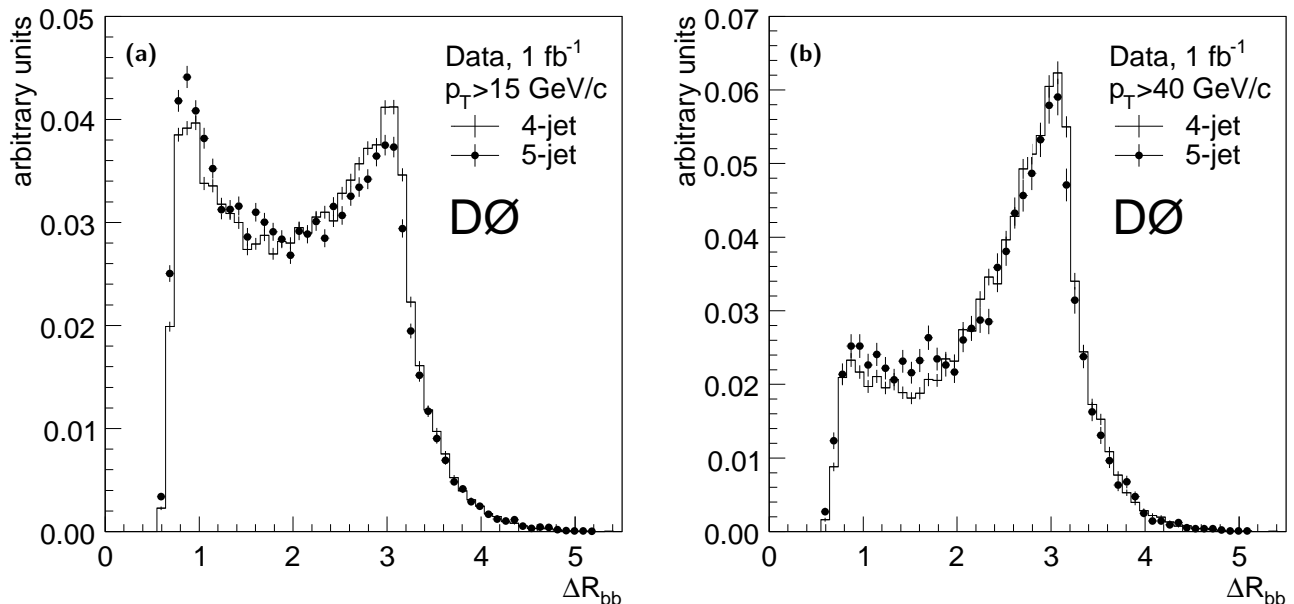


FIG. 5: ΔR between the two leading b -tagged jets in 4-jet and 5-jet events with (a) $p_T > 15$ GeV/ c ; (b) $p_T > 40$ GeV/ c . The peak near $\Delta R \approx \pi$ is dominated by direct $b\bar{b}$ production while the peak near $\Delta R \approx 1$ (twice the jet radius) is mainly $g \rightarrow b\bar{b}$. Displayed error bars represent statistical uncertainties only. Distributions are normalized to unit area.

One concern with basing the background distributions on a lower jet-multiplicity sample was that the relative contributions of different production diagrams might depend strongly on jet multiplicity. This was tested by examining distributions of the ΔR between the b jets. We expect a peak near π for $b\bar{b}$ produced in $2 \rightarrow 2$ hard scatters, whereas we expect a peak near one (twice the jet radius) for $b\bar{b}$ produced via gluon splitting, $g \rightarrow b\bar{b}$. This is illustrated for four and five jet events in Fig. 5. Figure 5(a) shows ΔR_{bb} for b jets with $p_T > 15$ GeV/ c while Fig. 5(b) is the ΔR_{bb} for b jets with $p_T > 40$ GeV/ c . The relative height of the two peaks depends strongly on the p_T requirement, but there is little difference between four- and five-jet events. The gluon-splitting contribution is significantly suppressed by increasing the b -jet p_T requirement from 15 to 40 GeV/ c .

The scheme for creating a background sample was developed in a relatively pure QCD multijet context. A “background” sample was constructed by adding the lowest p_T jet from five-jet events to four-jet events. The two sources of jets were matched together to ensure compatible phase-space configurations. The leading jets in each sample were required to have a difference in p_T (Δp_T) within 1 GeV/ c . Matches resulting in unphysical configurations (e.g., spatially overlapping jets) were rejected. The background event statistics were enhanced by running twenty times over the four- and five-jet samples. In each step the Δp_T requirement was relaxed by 1 GeV/ c .

One issue with this matching scheme is that an initial four-jet event might not have sufficient phase space

for an additional jet. Since QCD multijet events are not expected to contain significant missing transverse energy (\cancel{E}_T), the presence of \cancel{E}_T implies the presence of unreconstructed or mismeasured jets which makes these events more suitable for use in the background sample. However, badly mis-reconstructed events or events containing hard neutrinos can skew the phase space. Requiring the ratio of \cancel{E}_T to $H_{T4} \equiv \sum_{i=1}^4 p_{Ti}$ to be small reduced these contributions. Agreement between the “signal” (unadulterated) and “background” five-jet samples was best with $\cancel{E}_T > 5$ GeV/ c and $\cancel{E}_T/H_{T4} < 0.1$. Variations in this additional phase space selection were included in the systematic uncertainty evaluation [22].

The resulting events were compared with the five-jet sample as illustrated in Fig. 6. Reasonable agreement was achieved with the individual jet p_T distributions and with their sum. These manufactured background events are also compared against the five-jet events for several topological variables (defined in Sec. III E) in Fig. 7.

Both the original four-jet sample used to create these five-jet “background” events and the “signal” five-jet sample to which it was compared had little contamination from $t\bar{t}$ (0.2% and 0.7%, respectively), so this tests our ability to use one multijet sample to create a representation of a higher-multiplicity sample. This scheme was extended to produce the background sample for events with six or more jets. In this case, the lowest p_T jets were added to either four-jet (fifth and lower p_T jets) or five-jet (sixth and lower p_T jets) samples. There was no reason to prefer the four-jet-initiated background over the one built from a five-jet sample. Instead, an equal

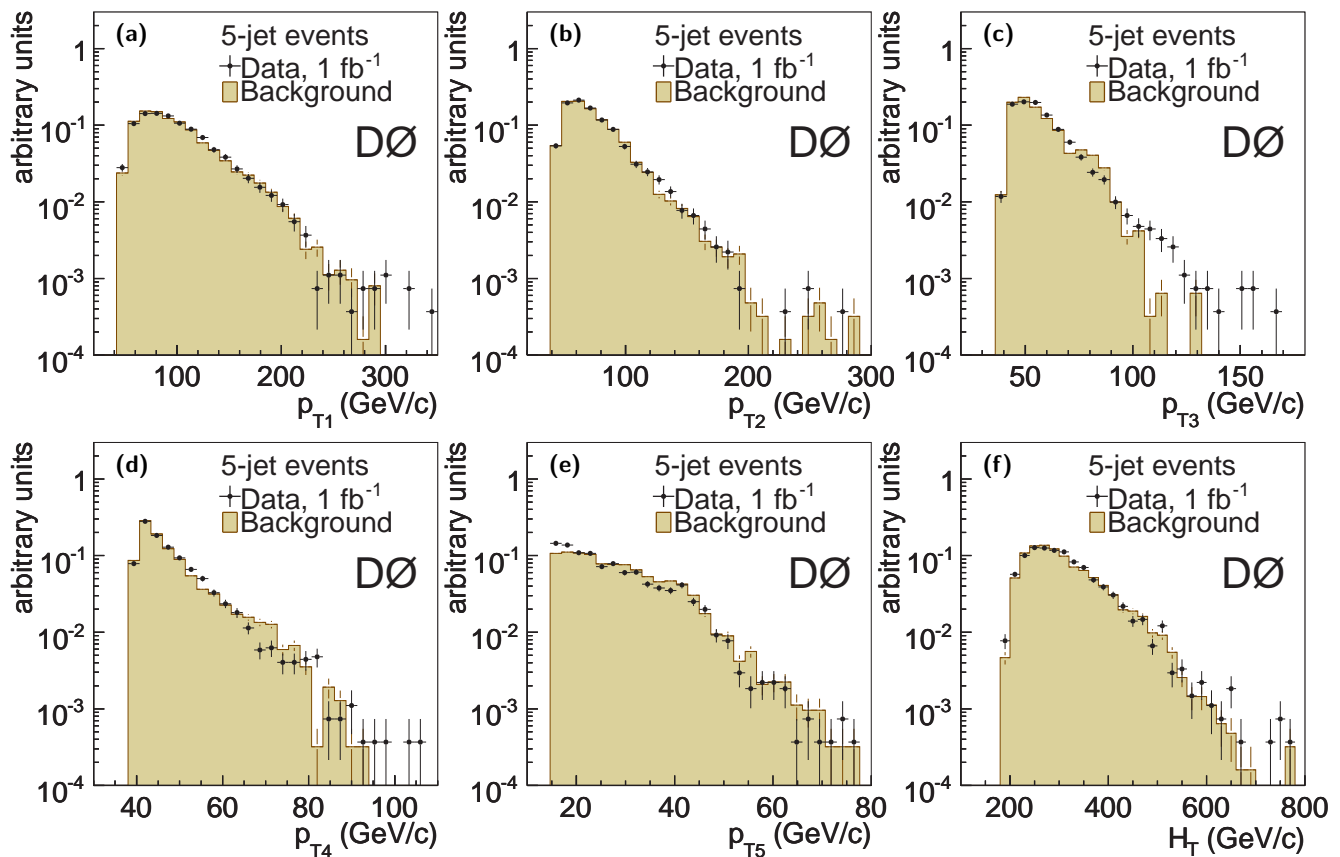


FIG. 6: Comparisons between the five-jet data and the background created from four-jet data for the p_T distributions of each jet (p_{T1} through p_{T5}) and for H_T . The leading four jets were required to have $p_T > 40$ GeV/ c . Displayed error bars represent statistical uncertainties only. Distributions are normalized to unit area.

mix of the two was used for the final background sample and the difference between the two separate background samples and the mixed sample was used when evaluating systematic uncertainties. Variations between the two samples as a function of H_T are shown in Fig. 8. Also shown is the change in the background due to systematic variations in the phase-space matching criteria described above.

C. Signal Model

The $t\bar{t}$ signal was simulated with the ALPGEN event generator. Two inclusive $t\bar{t}$ samples were used in this analysis: one with $m_t = 170$ GeV/ c^2 and one with $m_t = 175$ GeV/ c^2 [23]. PYTHIA, with the tune A parameter settings, was used for the parton shower, hadronization, and underlying event aspects. The resulting events were processed through a GEANT [24] simulation of the D0 detector and underwent the full reconstruction and analysis procedure. Information from data events selected by a random beam crossing trigger were overlaid on the simulated events to reproduce experimental conditions including detector noise and overlapping $p\bar{p}$ in-

teractions. The instantaneous luminosity distribution of the simulated events was weighted to match that of the triggered data.

Several additional corrections were applied to the simulated events. First, the event generator used the leading order (LO) parton distribution functions (PDF) from CTEQ6L1 [25, 26]. Events were reweighted to correspond to the CTEQ6.5M [27] PDF. Second, the default heavy-flavor fragmentation function in PYTHIA was reweighted to one that described the LEP e^+e^- data [28]. Additionally, the resolutions of reconstructed objects in the simulation were slightly better than those in the data, so the energies of jets, muons, and electrons were smeared to reproduce the resolutions observed in data [29]. The jet identification efficiency is slightly higher in the simulation than in data. Therefore, jets in the simulation were randomly removed to make the efficiencies agree.

D. Event Selection

Selection criteria were applied to triggered events to minimize background while retaining a relatively high signal efficiency. The selection criteria, together with

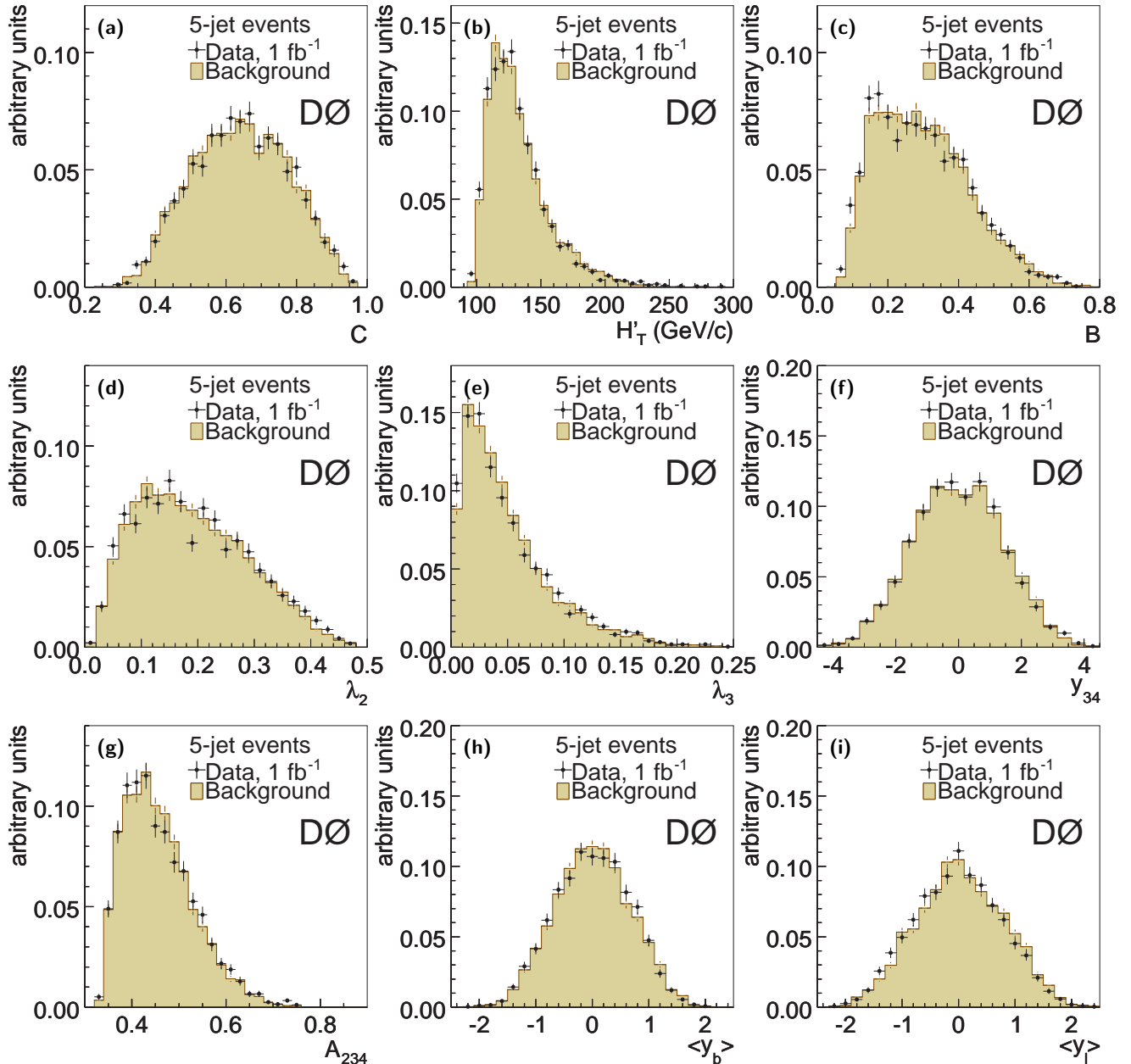


FIG. 7: Comparisons between the five-jet data and the background created from four-jet data for variables used in the likelihood discriminant. The leading four jets were required to have $p_T > 40$ GeV/ c . Displayed error bars represent statistical uncertainties only. Distributions are normalized to unit area.

the number of events after each cut, the cut efficiency ε , and the cumulative selection efficiency ε_{cum} , are presented in Table I. Values are given for the all-hadronic $t\bar{t}$ signal, for signal in all other $t\bar{t}$ decay channels, and for the data-based background. The signal fraction in the final selected sample corresponded to a purity of 12.5% (as found in Sec. IV A). As the background was derived from triggered data, the minimum set of requirements on that sample, which also included a reconstructed primary vertex with $|z_{\text{PV}}| < 35$ cm and ≥ 4 jets having $p_T > 15$ GeV/ c , are listed as the second line in Table I.

This corresponded to a starting signal-to-background ratio of approximately 1 : 7700.

Events with isolated high- p_T electrons and muons were removed to avoid overlap with other D0 $t\bar{t}$ cross section measurements [30, 31]. This requirement had little effect on the all-hadronic $t\bar{t}$ signal, but did remove a considerable number of events from the background.

Events considered in this analysis were required to have at least six jets. Each jet was required to be taggable, have $p_T > 15$ GeV/ c , and $|\eta| < 2.5$. Furthermore, at least four of the jets were required to have

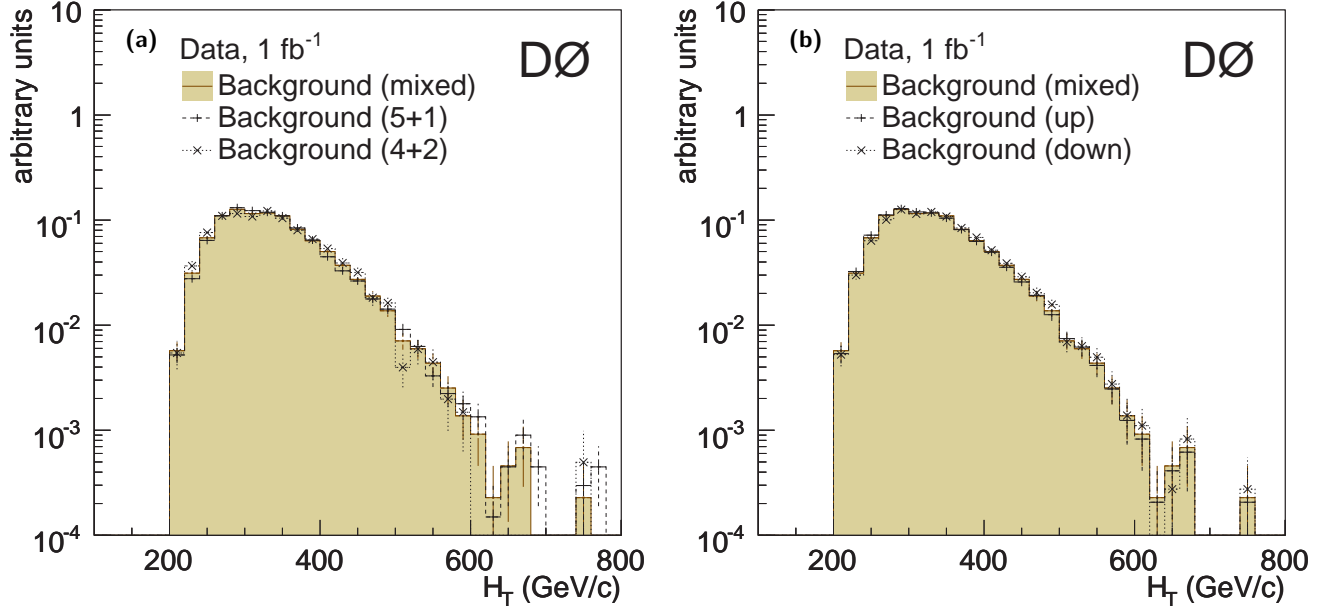


FIG. 8: Systematic variations in the background sample with six or more jets as a function of H_T . (a) Comparisons with the background samples created using only four-jet (4+2) or five-jet (5+1) events. (b) Comparisons including one-sigma systematic variations in the phase-space matching criteria. The leading four jets were required to have $p_T > 40$ GeV/c. Distributions are normalized to unit area.

TABLE I: The number of events after each selection requirement. Each selection is inclusive of the ones above it. Shown are the criteria, the number of events that pass the selection, the efficiency of the selection (ϵ), and the cumulative selection efficiency (ϵ_{cum}) for all-hadronic $t\bar{t}$, all other $t\bar{t}$ decay channels, and the data-based background. The $m_t = 175$ GeV/ c^2 sample was used for the signal expectation. Signal and background numbers have been adjusted, using the 12.5% signal fraction measured in this analysis, to sum to the number of candidate events selected in the data. Statistical uncertainties are included for the overall signal efficiency.

Selection	All Hadronic $t\bar{t}$			Other $t\bar{t}$			Background			Approx. S:B
	Num.	ϵ (%)	ϵ_{cum} (%)	Num.	ϵ (%)	ϵ_{cum} (%)	Num.	ϵ (%)	ϵ_{cum} (%)	
Total	3024	100.0	100.0	3712	100.0	100.0				
Trigger, vertex, ≥ 4 jets with $p_T > 15$ GeV/c	1663	55.0	55.0	773	20.8	20.8	18856263	100.0	100.0	1:7700
Lepton veto	1662	100.0	55.0	558	72.2	15.0	12679185	67.2	67.3	1:5700
≥ 6 jets with $p_T > 15$ GeV/c	913	55.0	30.2	165	29.6	4.5	1734595	13.7	9.2	1:1600
≥ 6 taggable jets with $p_T > 15$ GeV/c	628	68.8	20.8	60	36.3	1.6	506277	29.2	2.7	1:740
≥ 2 b-tagged jets with $p_T > 40$ GeV/c	150	23.8	4.9	13	21.8	0.4	2562	0.5	0.014	1:16
≥ 3 jets with $p_T > 40$ GeV/c	147	98.1	4.9	12	95.2	0.3	2059	80.4	0.011	1:13
≥ 4 jets with $p_T > 40$ GeV/c	122	83.2	4.0	9	70.3	0.2	920	44.7	0.0049	1:7
Efficiency	(4.04 \pm 0.02)%			(0.24 \pm 0.01)%						
Inclusive $t\bar{t}$ Efficiency	(1.94 \pm 0.01)%									

$p_T > 40$ GeV/c. At least two of these high- p_T jets were required to be b tagged. These additional jet requirements improve the signal-to-background ratio by a factor of 100.

In total, 1051 data events satisfy the selection criteria. The efficiency for all-hadronic $t\bar{t}$ events with $m_t = 175$ GeV/ c^2 is (4.04 \pm 0.02)% while the overall efficiency for inclusive $t\bar{t}$ events is (1.94 \pm 0.01)% (statistical uncertainties only). The equivalent efficiencies with $m_t = 170$ GeV/ c^2 are (3.65 \pm 0.04)% and (1.76 \pm 0.02)%,

respectively. Given these efficiencies and the standard model branching fractions, $\approx 93\%$ of the selected $t\bar{t}$ events are from the all-hadronic decay channel. The surviving leptonic $t\bar{t}$ events were primarily from the ℓ +jets ($\approx 60\%$) and τ +jets ($\approx 40\%$) decay channels. Few dileptonic events survived the full selection criteria ($\approx 0.05\%$ of $t\bar{t}$).

The expected signal-to-background ratio, given the 12.5% signal purity extracted during the cross section measurement, is 1 : 7.

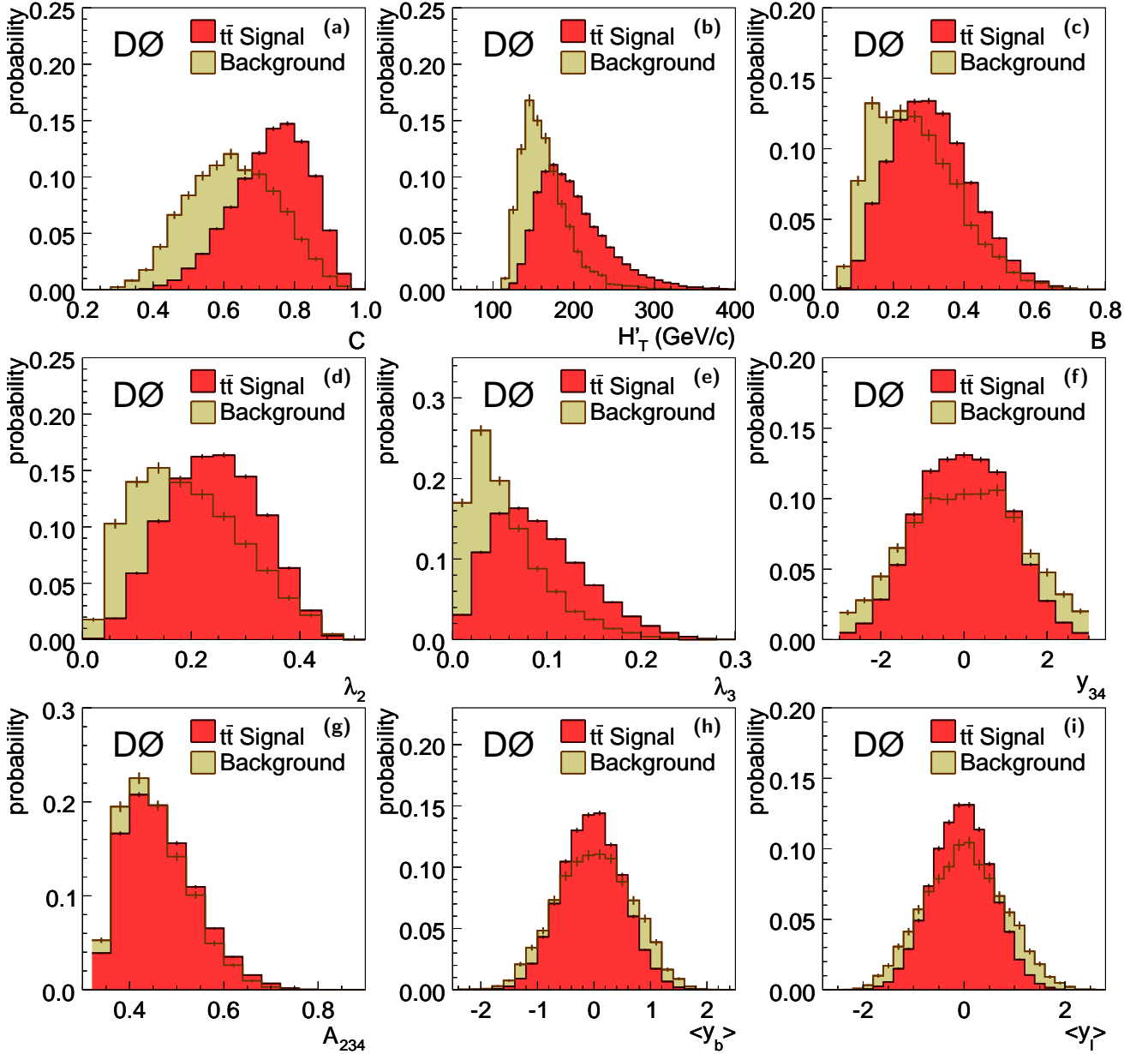


FIG. 9: Probability distributions for the variables input into the likelihood ratio. The signal distributions were extracted from the sample with $m_t = 175 \text{ GeV}/c^2$. Displayed error bars represent statistical uncertainties only.

E. Maximum Likelihood

A likelihood discriminant based on topological observables was constructed to separate the all-hadronic $t\bar{t}$ signal from the multijet background. The likelihood ratio, L , for an event i is defined as

$$L = \frac{L_S(i)}{L_S(i) + L_B(i)},$$

where

$$L_S(i) = \prod_{k=1}^{n_{\text{var}}} \mathcal{P}_{S,k}[x_k(i)]$$

for signal and similarly for background. Here, $\mathcal{P}_{S,k}$ is the signal probability density function, normalized to unit area, for the k th input variable x_k , and n_{var} is the number of variables. The TMVA [32] package was used to build the probability distributions and the resulting likelihood ratio.

The criteria for selection of observables to be input into the likelihood were: separation between signal and background, reasonable agreement in the five-jet background validation, little correlation with other chosen variables, and little dependence on jet energies (to minimize systematic uncertainty due to jet energy calibration). The following nine variables were used in the likelihood deter-

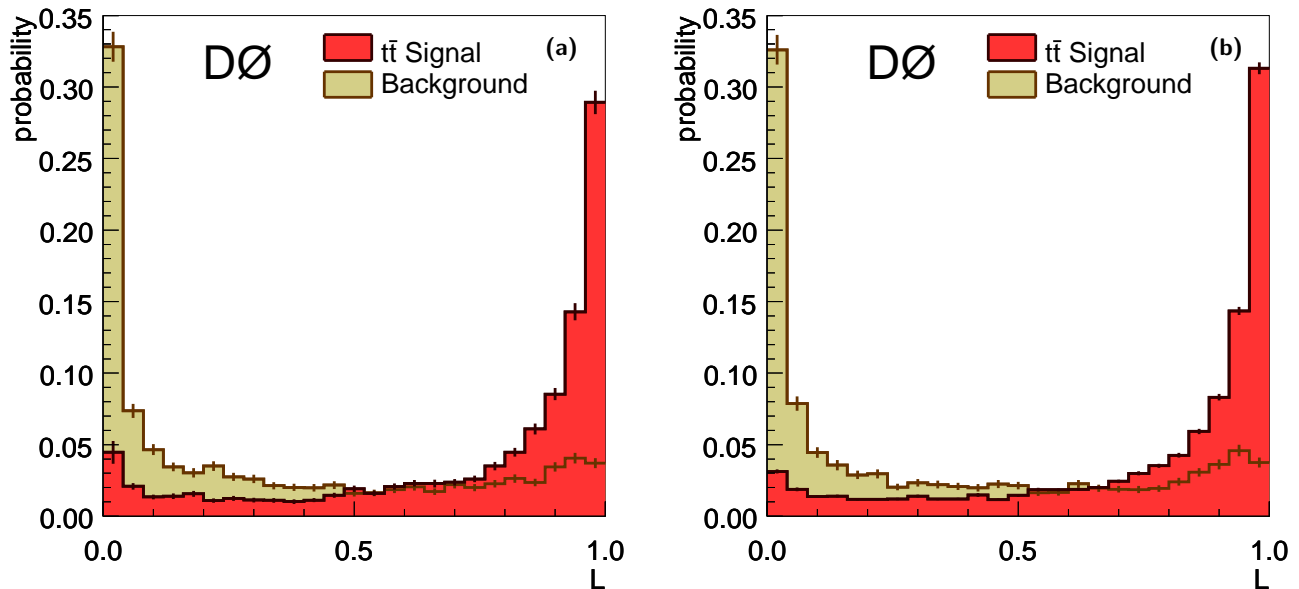


FIG. 10: Probability distributions from the likelihood function, L , for $t\bar{t}$ signal and the data-derived background. Displayed error bars represent statistical uncertainties only. (a) Signal sample with $m_t = 170$ GeV/ c^2 ; (b) $m_t = 175$ GeV/ c^2 .

mination and are shown for simulated signal and data-based background events in Fig. 9:

- C is the centrality defined as the scalar sum of jet p_T divided by the sum of jet energies;
- H'_T is the scalar sum of jet p_T excluding the two highest p_T jets;
- B is the ratio of the dijet mass of the two leading b -tagged jets to the total mass of all the jets;
- λ_2, λ_3 are the smallest two eigenvalues of the momentum tensor $M^{\alpha,\beta} = \sum_i p_i^\alpha p_i^\beta / \sum_i |\vec{p}_i|^2$ where i runs over the number of jets and $\alpha, \beta = 1, 2, 3$ denote the three spatial components of the jet momenta [33];
- y_{34} is the rapidity difference between the third and fourth leading jets;
- A_{234} is the p_T asymmetry between the second and third jet and the fourth jet defined as $(p_{T2} + p_{T3} - p_{T4}) / (p_{T2} + p_{T3} + p_{T4})$;
- $\langle y_b \rangle$ is the p_T -weighted average of the rapidities of the leading two b -tagged jets;
- $\langle y_l \rangle$ is the p_T -weighted average of the rapidities of the leading two light (not b tagged) jets.

Comparisons are shown in Fig. 7 for these variables in the five-jet background validation sample. The combined probability distributions for signal and background are shown in Fig. 10. The probability distributions and likelihoods were extracted independently for the $m_t = 170$ GeV/ c^2 and 175 GeV/ c^2 samples.

IV. RESULTS

A. Signal Fraction

The signal and background likelihood templates were fit to the likelihood output, shown in Fig. 10, for the selected data events using TMINUIT [34] from ROOT [35]. Results from the fit are shown in Fig. 11 and are in agreement with the data. The measured signal fractions are $(12.9 \pm 2.4)\%$ for $m_t = 170$ GeV/ c^2 and $(12.5 \pm 2.3)\%$ for $m_t = 175$ GeV/ c^2 . Given 1051 data candidate events, this results in 136 and 131 $t\bar{t}$ events, respectively. Distributions for the observables included in the likelihood, using the signal and background fractions from the fit, are shown in Fig. 12 for $m_t = 175$ GeV/ c^2 . There is reasonable agreement between the data candidates and the sum of signal and background, normalized to the fit results.

Jets in an event can be associated with the decays of individual top quarks. A χ^2 was constructed comparing the dijet masses with the W boson mass and the two bjj masses with each other. The combination with the lowest χ^2 value was chosen. The results for the dijet mass and the bjj mass are shown in Figs. 13(c) and (d). There is good agreement between data and the sum of signal and background. The comparison is also made in a region of phase space dominated by background ($L < 0.2$) and one which has a significantly larger signal fraction ($L > 0.8$), also shown in Fig. 13. The distributions were not renormalized. Both the background-dominated and signal-enhanced distributions show reasonable agreement between data and the sum of signal and background.

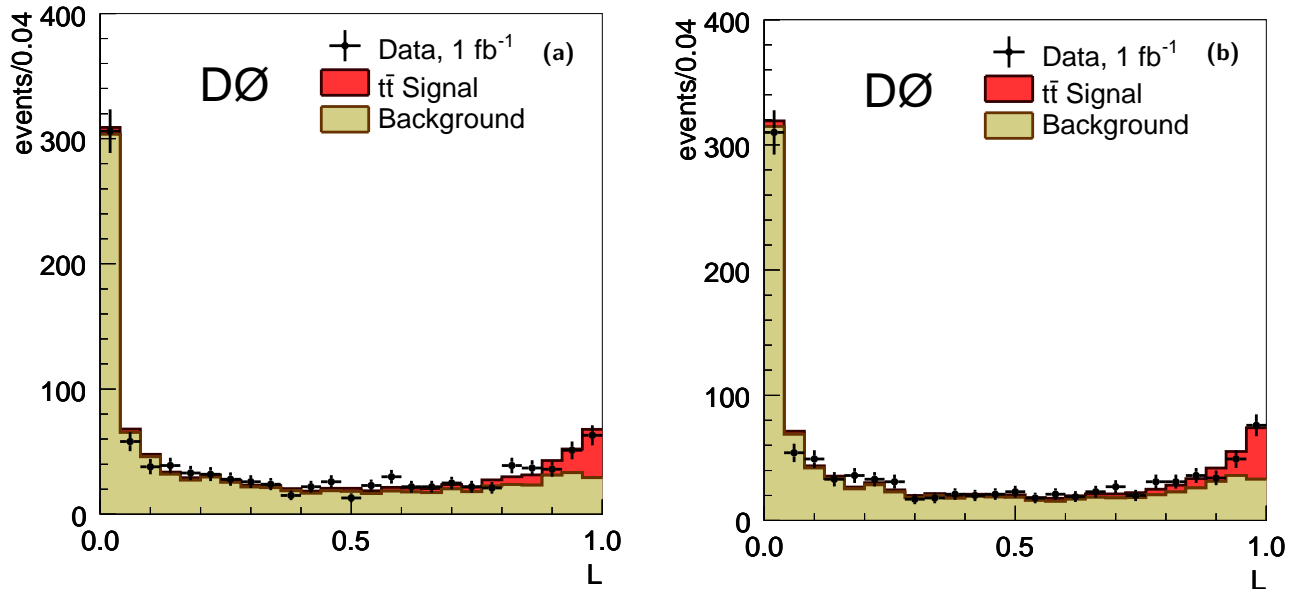


FIG. 11: Comparison of the distributions of likelihood output values, L , for the selected data candidates (points) with those from the $t\bar{t}$ signal and data-based background samples. Signal and background were fit to the data candidates and are presented with a normalization equal to the fit purity times the number of candidate events for the signal. Displayed error bars represent statistical uncertainties only. (a) Signal sample with $m_t = 170$ GeV/ c^2 ; (b) $m_t = 175$ GeV/ c^2 .

B. Systematic Uncertainties

The effects of systematic uncertainties and variations in input variables were studied using ensemble tests. Ten thousand pseudo-experiments were run for each source of uncertainty. Each pseudo-experiment drew events from the systematically-shifted signal and background distributions and was fit using the standard signal and background likelihood templates. With the exception of the two background-related systematics, all of the systematic uncertainties are associated with the signal simulation only. All systematic uncertainties on the $t\bar{t}$ production cross section measured with $m_t = 175$ GeV/ c^2 are summarised in Table II. Many of these are described in more detail in earlier sections of this paper.

This analysis relies on ALPGEN+PYTHIA for the $t\bar{t}$ signal model used to determine the selection efficiency (Table I) and the kinematic shapes included in the likelihood determination (Fig. 9). It is possible that the $t\bar{t}$ simulation does not properly reproduce the properties of the $t\bar{t}$ system. Other analyses in the lepton+jets and dilepton decay channels published by the D0 collaboration have found good agreement between the simulation and the reconstructed data [29, 30, 31, 36]. Nevertheless, the simulation might mis-estimate the jet multiplicity through differences in the QCD radiation or the underlying event. The measured fraction of reconstructed $t\bar{t}$ events (using the measured signal purities) with seven or more jets is 0.29 ± 0.04 . The signal events were weighted up and down by one standard deviation in the statistical

uncertainty on this ratio (15%). The entire analysis was repeated and the resulting difference in the mean cross section applied as a systematic uncertainty. The PDF in the simulation were also reweighted to correspond to CTEQ6.5M. The modified tolerance approach [27, 37] was used to estimate the effects of the PDF uncertainties on the measured cross section. Both of these uncertainties, along with those related to the reweighting of the heavy-flavor fragmentation function, luminosity profile, and vertex distribution; are listed as the signal model uncertainty in Table II.

The dominant sources of systematic uncertainty in the $t\bar{t}$ cross section measurement are the jet energy calibration (10.8%), construction of the data-based background (10.7%), b tagging (9.2%), and jet taggability (8.8%). The total systematic uncertainty is 20.5%.

C. Cross Section Measurement

The cross section is defined as

$$\sigma_{t\bar{t}} = \frac{fN}{\mathcal{L}\varepsilon},$$

where f is the measured fraction of $t\bar{t}$ signal, N is the number of selected data events, \mathcal{L} is the integrated luminosity, and ε is the inclusive $t\bar{t}$ efficiency given in Table I.

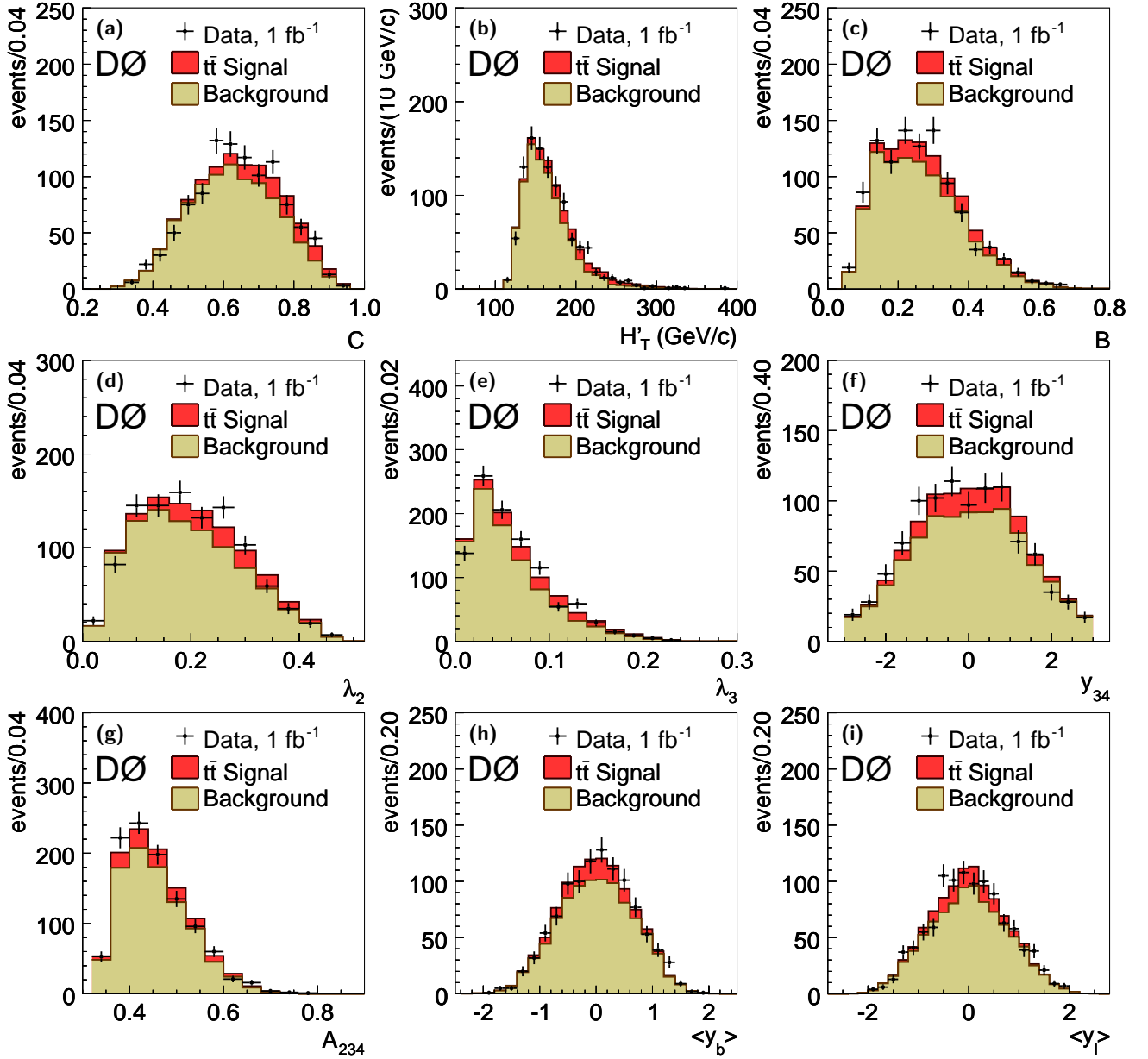


FIG. 12: Comparison between the data candidates and the sum of $t\bar{t}$ signal with $m_t = 175 \text{ GeV}/c^2$ and the data-based background for the variables used in the likelihood discriminant. Displayed error bars represent statistical uncertainties only.

This results in the following cross sections:

$$\sigma_{t\bar{t}}^{170 \text{ GeV}/c^2} = 7.9 \pm 1.5 \text{ (stat)} \pm 1.6 \text{ (sys)} \pm 0.5 \text{ (lum)} \text{ pb}$$

$$\sigma_{t\bar{t}}^{175 \text{ GeV}/c^2} = 6.9 \pm 1.3 \text{ (stat)} \pm 1.4 \text{ (sys)} \pm 0.4 \text{ (lum)} \text{ pb}$$

The statistical uncertainty includes the statistical uncertainties associated with the signal and background templates. The latter was determined by re-fitting the data 100,000 times while allowing the signal and background templates to vary according to their bin-to-bin statistical uncertainties. The resulting uncertainties are summarized in Table II. Figure 14 shows the SM prediction together with the measured cross section from this anal-

ysis. The SM expectation [6] is in agreement with the measured cross sections.

V. CONCLUSIONS

We presented the inclusive $t\bar{t}$ cross section measured in 1 fb^{-1} of $p\bar{p}$ interactions at $\sqrt{s} = 1.96 \text{ TeV}$. The cross section was extracted using high-multiplicity jet events, specifically events with at least six jets, two of them b tagged. A model of the multijet background was created from lower jet-multiplicity data. A likelihood discriminant was used to separate signal from back-

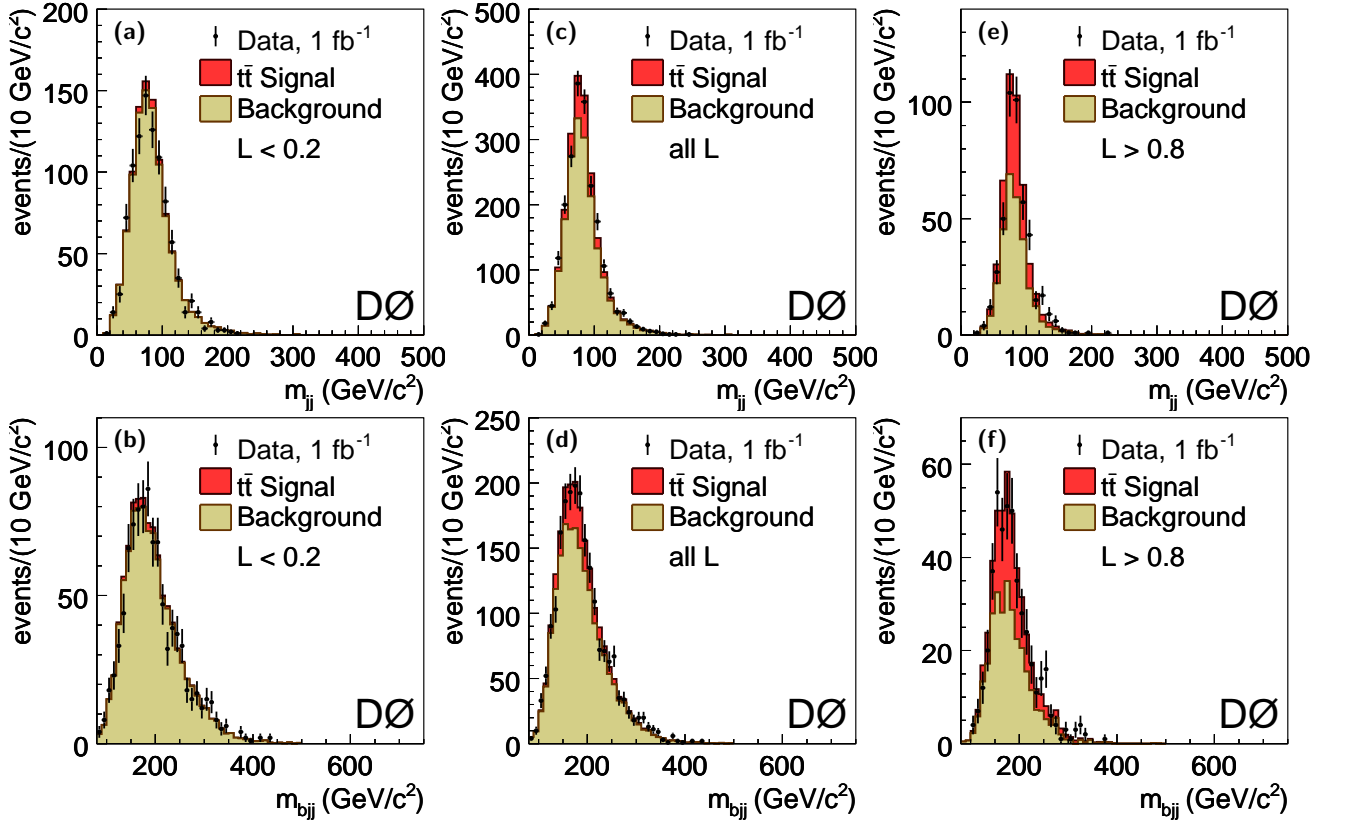


FIG. 13: Distributions for the reconstructed W boson (top row) and top quark (bottom row) masses using the $m_t = 175 \text{ GeV}/c^2$ signal sample. There are two entries per event. Displayed error bars represent statistical uncertainties only. (c, d) Result from the purity fit. (a, b) additionally requiring $L < 0.2$ to enhance background; (e, f) additionally requiring $L > 0.8$ to enhance signal.

TABLE II: Uncertainties on the $t\bar{t}$ cross section categorized by source for the result corresponding to $m_t = 175 \text{ GeV}/c^2$. The uncertainties with $m_t = 170 \text{ GeV}/c^2$ are similar.

Source	Uncertainty (%)
Candidate statistics	± 18.5
Background model	± 10.7
Background model statistics	± 3.8
Signal model	± 3.2
Signal model statistics	± 0.5
Trigger	$-2.0 \quad +3.9$
Jet identification efficiency	$-2.5 \quad +3.0$
Jet taggability	± 8.8
Jet energy calibration	± 10.8
Jet energy resolution	$-3.1 \quad +2.2$
b tagging	$-8.6 \quad +9.2$
Total statistical uncertainty	± 18.9
Total systematic uncertainty	± 20.5
Luminosity uncertainty	± 6.1

ground. The cross section was obtained from a likelihood fit to the discriminant distribution and was measured to be $7.9 \pm 2.2 \text{ pb}$ assuming $m_t = 170 \text{ GeV}/c^2$, and $6.9 \pm 2.0 \text{ pb}$ assuming $m_t = 175 \text{ GeV}/c^2$. Both results agree with theoretical expectations.

Acknowledgments

We thank the staffs at Fermilab and collaborating institutions, and acknowledge support from the DOE and NSF (USA); CEA and CNRS/IN2P3 (France); FASI, Rosatom and RFBR (Russia); CNPq, FAPERJ, FAPESP and FUNDUNESP (Brazil); DAE and DST (India); Colciencias (Colombia); CONACyT (Mexico); KRF and KOSEF (Korea); CONICET and UBACyT (Argentina); FOM (The Netherlands); STFC and the Royal Society (United Kingdom); MSMT and GACR (Czech Republic); CRC Program, CFI, NSERC and WestGrid Project (Canada); BMBF and DFG (Germany); SFI (Ireland); The Swedish Research Council (Sweden); and CAS and CNSF (China).

[a] Visitor from Augustana College, Sioux Falls, SD, USA.

[b] Visitor from Rutgers University, Piscataway, NJ, USA.

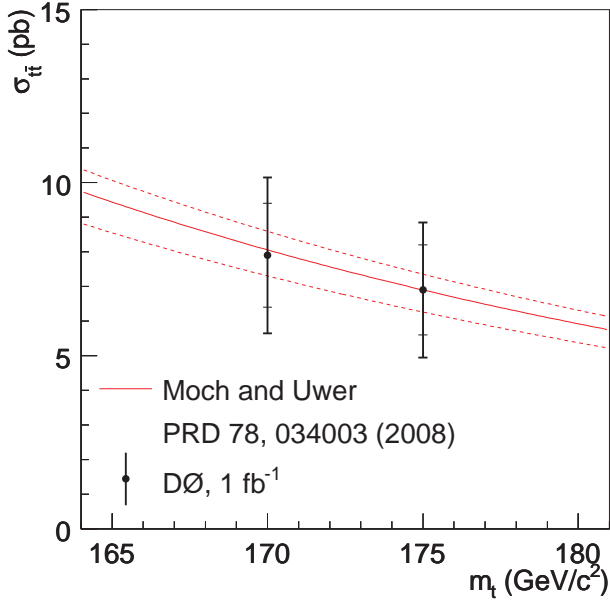


FIG. 14: The measured $t\bar{t}$ production cross section (\bullet markers) together with the SM prediction (solid line) and uncertainty (dashed lines) [6]. Shown with the cross section measurements are the corresponding statistical uncertainty (inner error bars) and total uncertainty (outer error bars).

- [c] Visitor from The University of Liverpool, Liverpool, UK.
[d] Visitor from SLAC, Menlo Park, CA, USA.
[e] Visitor from Centro de Investigacion en Computacion - IPN, Mexico City, Mexico.
[f] Visitor from ECFM, Universidad Autonoma de Sinaloa, Culiacán, Mexico.
[g] Visitor from Universität Bern, Bern, Switzerland.
[h] Visitor from Universität Zürich, Zürich, Switzerland.
- [1] Tevatron Electroweak Working Group and CDF and D0 Collaborations, arXiv:0903.2503 [hep-ex].
[2] W.-M. Yao *et al.* [Particle Data Group], *J. Phys. G* **33**, 1 (2006).
[3] M. Beneke *et al.*, arXiv:hep-ph/0003033.
[4] V. M. Abazov *et al.* [D0 Collaboration], *Phys. Rev. D* **76**, 072007 (2007).
[5] T. Aaltonen *et al.* [CDF Collaboration], *Phys. Rev. D* **76**, 072009 (2007).
[6] S. Moch and P. Uwer, *Phys. Rev. D* **78**, 034003 (2008).
[7] N. Kidonakis and R. Vogt, *Phys. Rev. D* **78**, 074005 (2008).
[8] T. Sjöstrand *et al.*, *Comput. Phys. Commun.* **135**, 238 (2001).
[9] G. Corcella *et al.*, *J. High Energy Phys.* **0101**, 010 (2001).
[10] M. L. Mangano *et al.*, *J. High Energy Phys.* **0307**, 001 (2003).

- [11] R. Field and R. C. Group, arXiv:hep-ph/0510198.
[12] V. M. Abazov *et al.* [D0 Collaboration], *Nucl. Instrum. Methods in Phys. Res. A* **565**, 463 (2006).
[13] Pseudorapidity η is defined as $\eta = -\ln[\tan(\theta/2)]$, where θ is the polar angle with respect to the proton beam direction, with origin at the center of the detector.
[14] S. Abachi *et al.* [D0 Collaboration], *Nucl. Instrum. Methods in Phys. Res. A* **338**, 185 (1994).
[15] T. Andeen *et al.*, FERMILAB-TM-2365 (2007).
[16] G.C. Blazey *et al.*, in *Proceedings of the Workshop: QCD and Weak Boson Physics in Run II*, edited by U. Baur, R.K. Ellis, and D. Zeppenfeld, Fermilab-Pub-00/297 (2000).
[17] T. Speer *et al.*, *Nucl. Instrum. Methods in Phys. Res. A* **566**, 149 (2006).
[18] V. M. Abazov *et al.* [D0 Collaboration], *Phys. Rev. D* **74**, 112004 (2006).
[19] Rapidity is defined as $y = -\ln[(E+p_z)/(E-p_z)]$, where E is the energy and p_z is the momentum along the proton beam direction. ϕ is defined as the azimuthal angle in the plane transverse to the proton beam direction.
[20] J. Hegeman, *J. Phys. Conf. Ser.* **160**, 012024 (2009).
[21] T. Scanlon, Ph.D. thesis, Imperial College London [Institution Report No. FERMILAB-THESIS-2006-43, 2006].
[22] \cancel{E}_T/H_{T4} was varied between 0.12 and 0.08, covering 68% CL, to allow more or less phase space for additional jets.
[23] Two top quark mass values were considered since the world-average mass varied between 170.9 ± 1.8 GeV/ c^2 and 174.2 ± 3.4 GeV/ c^2 during the time period covered by this analysis.
[24] R. Brun and F. Carminati, CERN Program Library Long Writeup W5013, 1993 (unpublished).
[25] J. Pumplin *et al.*, *J. High Energy Phys.* **0207**, 012 (2002).
[26] D. Stump *et al.*, *J. High Energy Phys.* **0310**, 046 (2003).
[27] J. Pumplin *et al.*, *J. High Energy Phys.* **0702**, 053 (2007).
[28] Y. Peters, K. Hamacher, and D. Wicke, FERMILAB-TM-2425-E (2006).
[29] V. M. Abazov *et al.* [D0 Collaboration], *Phys. Rev. D* **78**, 012005 (2008).
[30] V. M. Abazov *et al.* [D0 Collaboration], *Phys. Rev. Lett.* **100**, 192004 (2008).
[31] V. M. Abazov *et al.* [D0 Collaboration], *Phys. Lett. B* **679**, 177 (2009).
[32] A. Hocker *et al.*, arXiv:physics/0703039.
[33] Aplanarity is defined as $(3/2)\lambda_3$ and sphericity as $(3/2)(\lambda_2 + \lambda_3)$.
[34] F. James and M. Roos, *Comput. Phys. Commun.* **10**, 343 (1975).
[35] R. Brun and F. Rademakers, *Nucl. Instrum. Methods in Phys. Res. A* **389**, 81 (1997).
[36] V. M. Abazov *et al.* [D0 Collaboration], *Phys. Rev. Lett.* **103**, 092001 (2009).
[37] D. Bourilkov, R. C. Group, and M. R. Whalley, arXiv:hep-ph/0605240.